SP Science Press

ARTICLE

Graphene Size Dependent Hardness and Strengthening Mechanisms of Cu/Graphene Composites: A Molecular Dynamics Study

Zhang Shuang[1],   Chang Guo[1],   Li Liang[1],   Li Xiang[1],   Peng Haoran[1],   Chen Kaiyun[1],
Yang Nan[2],   Huo Wangtu[1]

[1] Advanced Materials Research Center, Northwest Institute for Nonferrous Metal Research, Xi`an 710016, China; [2] United Technology Center, Western Metal Materials Co., Ltd, Xi`an 710201, China

Abstract: The extraordinary strength of metal/graphene composites is significantly determined by the characteristic size, distribution and morphology of graphene. However, the effect of the graphene size/distribution on the mechanical properties and related strengthening mechanisms has not been fully elucidated. Herein, under the same volume fraction and distribution conditions of graphene, molecular dynamics simulations were used to investigate the effect of graphene sheet size on the hardness and deformation behavior of Cu/graphene composites under complex stress field. Two models of pure single crystalline Cu and graphene fully covered Cu matrix composite were constructed for comparison. The results show that the strengthening effect changes with varying the graphene sheet size. Besides the graphene dislocation blocking effect and the load-bearing effect, the deformation mechanisms change from stacking fault tetrahedron, dislocation bypassing and dislocation cutting to dislocation nucleation in turn with decreasing the graphene sheet size. The hardness of Cu/graphene composite, with the graphene sheet not completely covering the metal matrix, can even be higher than that of the fully covered composite. The extra strengthening mechanisms of dislocation bypassing mechanism and the stacking fault tetrahedra pinning dislocation mechanism contribute to the increase in hardness.

Key words: Cu/graphene composites; graphene size; hardness; strengthening mechanism; molecular dynamics

Graphene-reinforced metallic matrix (metal/graphene) composites have garnered significant attention owing to the exceptional mechanical properties of graphene, such as high strength and flexibility[1–5]. Recently, graphene characteristic design[6], i.e. adjusting the size[7–8], distribution[9], and morphology[10–11] of graphene without a change in constituents, has been proved to be a strategy to enhance strengthening efficiency. The introduction of graphene results in either a metal/graphene interface or precipitate-like structure relying on the size of graphene, and the ability to block dislocation propagation, resulting from dislocation-interface/precipitate interaction, determines the mechanical behavior of metal/graphene materials[12]. The related strengthening mechanisms[13–14], i. e., interface strengthening and Orowan streng-

thening, both contribute to the improvement in strength. Although the interface strengthening and Orowan strengthening have been well understood by extensive experiments and atomistic simulations in the past few decades, the question of how to balance the graphene size/distribution dependent strengthening mechanisms to realize the optimal strengthening efficiency has not been fully elucidated[15].

Previously, the influence of graphene sheet size on the mechanical properties and deformation behavior of metal/graphene has been extensively explored. Zhao et al[16] reported that a good balance between strength and ductility can be achieved using the largest sheet size of reduced graphene oxide (RGO) in experiments. Yang et al[17] found that the yield strength and fracture strength can be enhanced by increasing

the sheet size of graphene single-layers in bio-inspired metal/ graphene nanocomposites using molecular dynamics (MD) simulations. Copper-plated 6061 aluminum matrix composites reinforced by larger-sized graphene achieved a favorable combination of high tensile strength (218 MPa) and fracture strain (17.2%) [17]. Nanocarbon architecture engineering from carbon nanotubes (CNTs) to graphene nanoribbon (GNR) with large aspect ratio leads to the strength-ductility synergy of GNR/Al, obtaining a better strengthening effect[11,18]. A strengthening mechanism transition from load transfer (by sunk dislocation) to Orowan mechanism was demonstrated, which was closely associated with the aspect ratio or length of reinforcements (CNTs, CNT-RGO network and Cu_2O) in metal/graphene composites[19–20]. Shuang et al[21] illustrated different dislocation interaction behavior using periodic graphene and free graphene. They showed that dislocations could be transmitted across free graphene, whereas the transmission was very difficult for periodic graphene, thus the strengthening effect of free graphene was less obvious than that of the periodic case. Furthermore, when graphene strengthening effect transitioned from interface hardening to precipitate hardening, it led to a reduced strengthening effect[12]. In addition, Zhao et al[8] revealed that the strength of RGO-Al composite pillars increased with decreasing the RGO sheet size. The strength and hardness of the bio-inspired nanocomposites decreased with the increase in the size of graphene layers[22]. Nanoindentation force tends to increase with decrease in the graphene sheet size when nanoindentation indenter is not in contact with the graphene sheets, and when the indenter is in contact with the graphene sheets, it is the opposite case[23].

The size/morphology of graphene significantly influence its physical and mechanical properties[24–27]. In zigzag GNRs (ZGNRs), as the size or width of ZGNRs increases, the elastic modulus increases while the ultimate failure stress and strain decrease[25]. The rigidity is found to be dependent on the size and the shape of graphene sheets[27], suggesting that the smaller the graphene sheet, the lower the bending rigidity. Graphene can change the stress distribution along the graphene layers and release the high stress in the near-graphene field[7]. As mentioned above, variations in the size/ morphology of graphene greatly influence its in-plane deformation and load-bearing effects. Most studies typically choose rectangular or circular shapes as the standard graphene structure/morphology when investigating strengthening mechanisms. However, the growth morphology of single crystalline graphene, which is actually hexagonal[28], has been rarely reported, and the specific interactions at the dislocation-graphene/metal interface remain unclear.

Based on the morphology and distribution of graphene[28–29], without changing the distribution and concentration, i. e., the reported optimal 5vol% graphene[15,30], MD simulations were used to investigate the impact of graphene sheet size on the hardness and deformation behavior of Cu/graphene composites under a complex stress field via nanoindentation. Two models, one of pure Cu crystal and the other of

graphene completely covered Cu crystal plane, were established for comparison. The deformation strengthening effects were analyzed by varying graphene sheet size.

1 Simulation Method

1.1 Interatomic potentials and analysis

Hybrid pair-style interactions were adopted. The embedded atom method developed by Foiles et al[31] was used to describe the interatomic interactions between Cu atoms, which can accurately capture the mechanical behavior[32–33]. The adaptive intermolecular reactive bond order potential was used to describe the covalent interactions of C-C bonds[34]. Additionally, the 12-6 Lennard-Jones (LJ) potential was efficient for describing the van der Waals interactions between graphene and Cu, and the corresponding LJ potential parameters[35] are $\sigma_{(C-Cu)}$=0.30825 nm and $\varepsilon_{(C-Cu)}$=0.02578 eV, with a cutoff radius r_c=2.5σ.

The Ovito visualization software[36] was employed to analyze atomic microstructures. Specifically, the common neighbor analysis (CNA) method[37] effectively characterizes the local crystal structures of atoms. It identifies crystalline structures such as face-centered cubic (fcc), body-centered cubic, hexagonal close-packed (hcp), icosahedron and other disordered and unidentifiable atomic structures. Additionally, atomic strain analysis[38–39] was utilized to generate color-coded strain maps, providing an intuitive measure for crystal plastic deformation. These strain maps reveal the extent of atomic shear strain induced during deformation. Furthermore, Dislocation analysis (DXA) [40] was employed. It determines the Burgers vector direction and magnitude, facilitating direct observation of dislocation motion and interactions during dynamic evolution processes. The DXA also yields the total dislocation line length and the lengths of various dislocation types. Therefore, the specific dislocation density can be calculated as follows: ρ_{dis}=dislocation line length/box volume, which is crucial for analyzing the role of dislocations during deformation.

1.2 Simulation models

All simulations were performed by the large-size atomic/ molecular massively parallel simulator (LAMMPS) [41]. The dimensions of the Cu/graphene composite model were 19.43 nm×22.58 nm×23.80 nm, and the graphene layer was positioned at 6 nm away from the z-axis surface. The coordinate system of the model along the x, y and z axes corresponded to [1$\bar{1}$0], [11$\bar{2}$] and [111] crystallographic orientations of Cu, respectively. Periodic boundary conditions were applied along the x and y axes, and a free boundary was used along z-axis. These specific nanoindentation models of Cu/graphene composites are displayed in Fig. 1. Purple and blue represent graphene and crystalline Cu, respectively. Each graphene sheet has a hexagonal shape with the radius denoted as r_g, as shown in Fig. 1a_1. To assess the coverage relationship between each graphene sheet and the matrix surface, the area ratio (s) of each graphene sheet to the matrix surface was used as the parameter describing the graphene size, which is
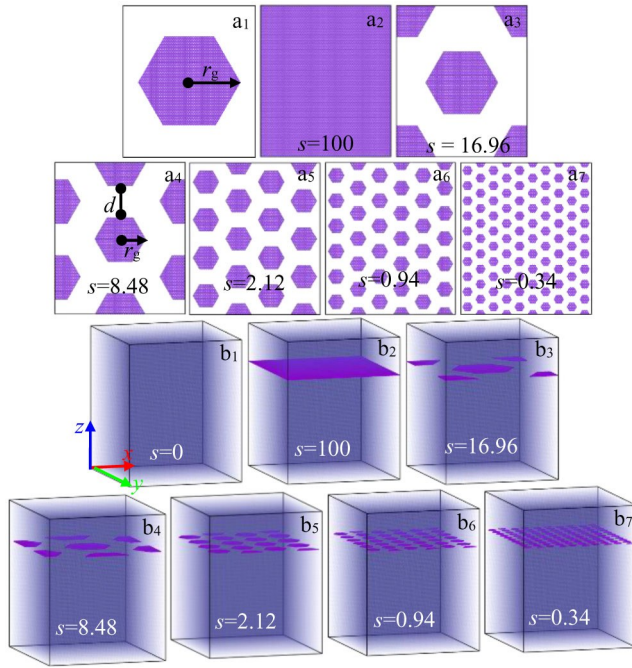
Fig.1 Nanoindentation models of Cu/graphene composites with different graphene sheet sizes: (a_1–a_7) graphene configuration and (b_1–b_7) Cu/graphene composites

labelled in the model. Additionally, the ratio (l) of the graphene sheet radius r_g to the graphene sheet spacing (d) reflects the distribution of the graphene layer on the matrix surface, which has been obtained by Zeng et al[29]. The configurations of the graphene layer with varying sheet sizes, under a fixed graphene content of 5vol% and similar distribution, are shown in Fig.1a_3–1a_7. To investigate the effect of graphene size variation on the mechanical properties of the composite materials, two models were established for comparison: pure Cu crystal ($s=0$) and graphene completely covered Cu crystal plane ($s=100$, Fig.1a_2). Fig.1b_1–1b_7 show the Cu/graphene models with different graphene sizes. Specific parameter details are provided in Table 1.

1.3 Nanoindentation simulations

During the indentation process, a complex stress field forms at the tip of the indenter, causing dislocations to be emitted beneath the indenter. This approach enables the measurement of hardness and the observation of dislocation-graphene interactions[42]. The nanoindentation method in LAMMPS employs a virtual spherical indenter to apply pressure to the model surface. The entire nanoindentation process consists of

Table 1 Specific parameters of graphene sheets in each model

Graphene sheet number	r_g/nm	d/nm	s/%	l
2	5.4	6.7	16.96	-
4	3.8	4.7	8.48	0.81
16	1.9	2.4	2.12	0.79
36	1.26	1.6	0.94	0.79
100	0.76	0.94	0.34	0.81

two stages: indentation and unloading. The schematic diagram of the nanoindentation simulation is shown in Fig.2a. The repulsive force (F) of the indenter during the MD simulation process is given as follows[41]:

$$F(r)=-K(r-R)^2 \quad r<R$$
$$F(r)=0 \quad r \geqslant R \tag{1}$$

where K represents the specified force constant (chosen as 10 μm·nm^{-2}); r denotes the distance from an atom to the center of the indenter; R corresponds to the radius of the spherical indenter. The bottom layers of atoms (approximately 1 nm in thickness) are fixed as the substrate, while the remaining atoms belong to the mobile Newtonian region. Within this region, atoms follow Newton's second law of motion.

The timesteps was 1 fs. Before the indentation loading, the MD models were relaxed by the conjugate gradient method and then equilibrated in the NPT ensemble at 300 K using the Nose-Hoover thermostat for 100 ps to approach zero stress in the x and y directions. Then, the NVE ensemble was used during the indentation process, and the temperature was controlled by resetting the temperature of a group of atoms via explicitly rescaling their velocities. The spherical radius of the indenter was set to 5 nm. An indentation speed of 0.01 nm·ps^{-1} was chosen. The temperature during the nanoindentation process was maintained at 300 K. The chosen indentation depth (h) was 3.25 nm, approximately 1/7 of the model's thickness, avoiding substrate effects.

The hardness calculation follows commonly used methods from Ref.[43]. The schematic evolution of the contact surface beneath the indenter during the indentation process is depicted in Fig.2b. For a spherical indenter, the indentation depth is much smaller than the indenter radius (R). Eq.(2 – 3) [44] accurately describe the contact area (A) and the corresponding contact stress (P), respectively, which are used to characterize the initial dislocation nucleation event beneath the indenter.

$$A=2\pi Rh \tag{2}$$
$$P=F/A \tag{3}$$

When the indentation depth becomes larger, the average contact stress (P_{AVG}) and the contact projected area (A_c) can be calculated by Eq.(4–5), respectively[45–46]. The average contact stress reflects the material response in the loading direction
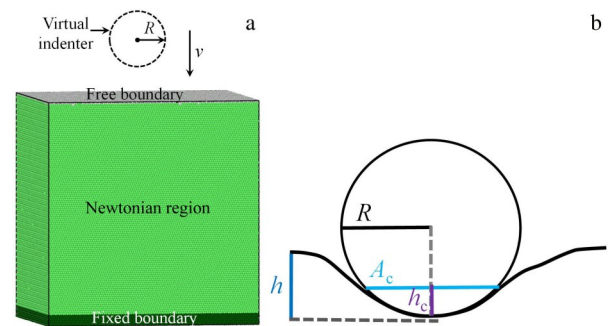

Fig.2 Schematic diagrams of nanoindentation simulations (a) and evolution under the indenter during the nanoindentation process (b)

and is defined as the ratio of the load to the contact projected area:

$$P_{AVG}=F/A_c \tag{4}$$

$$A_c=\pi(2R-h_c)\,h_c \tag{5}$$

Since the post-indentation sample surface is non-smooth and exhibits some pile-up around the indenter, it is challenging to directly extract the true contact depth (h_c). Therefore, the contact projected area is often approximated by the following expression[43]:

$$A_c=\pi(2R-h)h \tag{6}$$

Furthermore, the nanoindentation hardness is defined as the average contact stress (P_{AVG}) corresponding to the maximum load (F_{max})[45].

2 Results and Discussion

2.1 Nanoindentation force-depth curves

Fig. 3a depicts the load-depth curves along *z*-axis obtained from nanoindentation simulations on Cu/graphene models with different graphene sheet sizes and comparison group under identical indentation conditions. The average contact stress during the indentation process is obtained by Eq. (4–6), and the resulting curve of average contact stress as a function of indentation depth is illustrated in Fig. 3b. According to the interaction behavior between dislocations and graphene during the indentation process, the indentation process can be divided into three stages. The first stage (I) is the elastic deformation stage of the model until the initial dislocation nucleation event occurs beneath the indenter (depth≈0.6 nm). The second stage (II) is graphene layer interaction before contact with dislocations (depth≈0.6−1.16 nm), during which
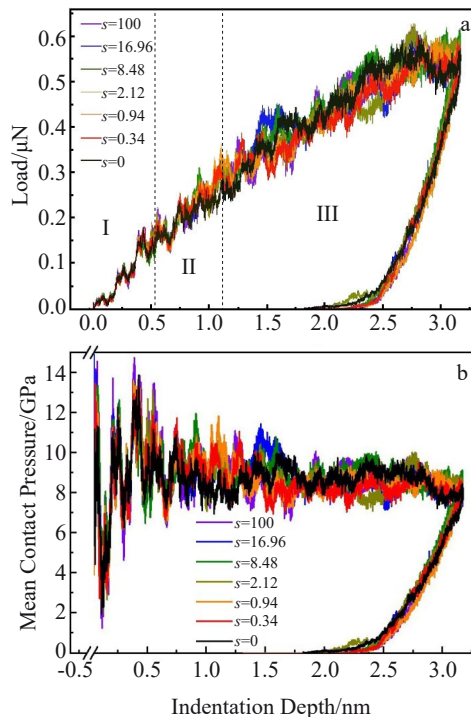
the graphene layers mainly play a role in hindering/obstructing dislocation movement. The third stage (III) occurs when the dislocations reach the graphene layers (depth≈1.16–3.25 nm), where the graphene layers interact with the dislocations.

The hardness or average stress at each stage can be calculated according to the load-depth curves and average contact stress curves, as shown in Fig. 4. Fig. 4a displays the hardness of different models in the second stage. Firstly, by comparing the hardness of different models, it is evident that the Cu/graphene composite with a graphene sheet size of *s*=8.48 exhibits the highest hardness, which is higher than that of the Cu/graphene composite with fully covered graphene interface. Secondly, all models added with graphene layers show higher hardness than the pure Cu model. These results indicate that in the second stage, the graphene layers hinder or obstruct dislocation motion. As the indentation depth increases and enters the third stage, to measure the combined contribution of deformation behavior involved in the indentation process to hardness/stress, the average contact stress of different models in the third stage is statistically analyzed and plotted, as shown in Fig. 4b. By comparison, the model with *s*=8.48 also exhibits the highest average contact stress, which is still higher than that of the Cu/graphene composite with fully covered graphene interface, indicating that the Cu/graphene composite with *s*=8.48 has the best comprehensive mechanical properties. The average contact stress of other models is lower than that of the Cu/graphene composite with fully covered graphene interface, indicating that the strengthening effect of these graphene sheet sizes is

Fig.3 Load-indentation depth curves (a) and average contact stress versus indentation depth curves (b)
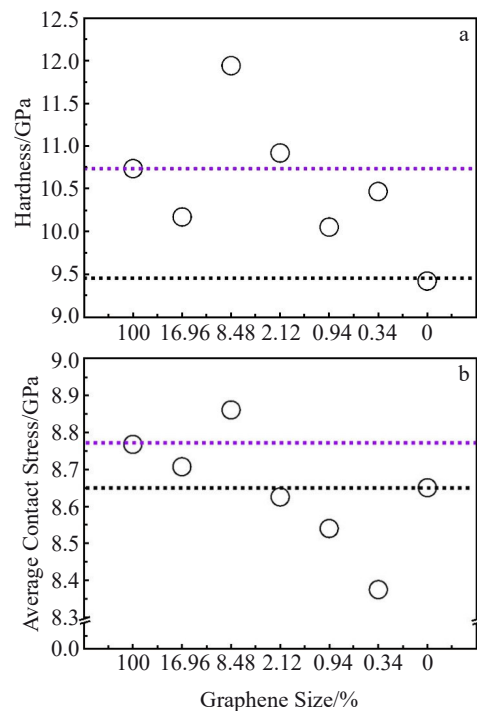

Fig.4 Hardness in the second stage (a) and average contact stress in the third stage (b) for different models

not as good as that of the average contact stress with fully covered graphene interface. Additionally, the average contact stress of the pure Cu model is also at a relatively high level at this stage, but the microstructure reveals that dislocations have already reached the bottom of the model, resulting in a significant hard substrate effect. Therefore, the average contact stress of the pure Cu model at this stage is not analyzed in detail.

2.2 Nucleation and evolution of dislocation during the indentation process

To clarify the effect of the graphene sheet size on the mechanical properties of Cu/graphene composites, it is essential to focus on how the interaction between dislocations and graphene, influenced by the graphene sheet size, governs the hardness under current indentation conditions. Therefore, a microstructural analysis was conducted. Fig.5–Fig.7 illustrate the microstructural evolution at the initial dislocation nucleation moment below the indenter (approximately 0.6 nm) and at indentation depths of 1.16 and 3.25 nm. The atomic structures are visualized by CNA coloring, in which fcc structure atoms are removed, hcp structure atoms render semi-transparent, and graphene sheet atoms are colored as purple for clarity. Fig. 5 shows the initial dislocation nucleation behavior beneath the indenter in different models, which generally occurs at an indentation depth of approximately 0.6 nm, providing insights into the early stage of plastic deformation. Fig.6 presents the microstructure at an indentation depth of 1.16 nm, corresponding to the moment when dislocations in the pure Cu model reach the graphene layer (indicated by the purple dashed line). By observing the dislocation emission and propagation behavior in the pure Cu model and the strengthening behavior caused by the graphene sheet, it is evident that dislocations beneath the indenter are either about to touch or have just touched the graphene sheets in the Cu/graphene composites, indicating that the graphene sheets act as barriers to dislocation motion. Notably, in the model with s=16.96, dislocations are present below the graphene sheets, which is due to the nucleation of dislocations from the edges of the Cu/graphene interface rather than

Fig.6 Microstructure evolution behavior at the indentation depth of 1.16 nm in Cu/graphene models with different graphene sizes: (a) s=0, (b) s=16.96, (c) s=8.48, (d) s=2.12, (e) s=100, (f) s=0.94, and (g) s=0.34

propagation from beneath the indenter. At an indentation depth of 3.25 nm (Fig.7), dislocations in the pure Cu model (s=0) have extended to the bottom of the model, while in the Cu/graphene model with fully covered graphene interface (s=100), dislocations are completely blocked above the graphene layer, demonstrating the strong dislocation blocking effect and load-bearing capacity of the graphene layer. In the remaining Cu/graphene models, dislocations are formed below the graphene sheet, which may result from various mechanisms such as dislocation bowing out between adjacent graphene sheets, dislocation slip through the graphene sheets, dislocation bypassing or dislocation cutting through the graphene sheets, or dislocation nucleation from the Cu/graphene interface. These possible deformation mechanisms can either strengthen or weaken the overall performance of the Cu/graphene composite materials.

The primary deformation carriers, i. e., dislocations, in different models during the indentation process were analyzed. Fig.8 shows the variation of total dislocation density with indentation depth. The total dislocation density in all models gradually increases with increasing indentation depth, indicating that the indentation process involves significant dislocation activity and interactions. Notably, there is an
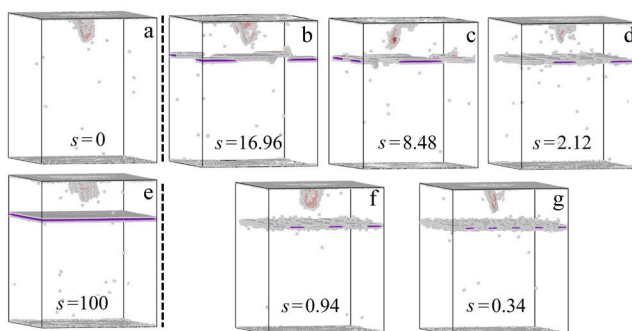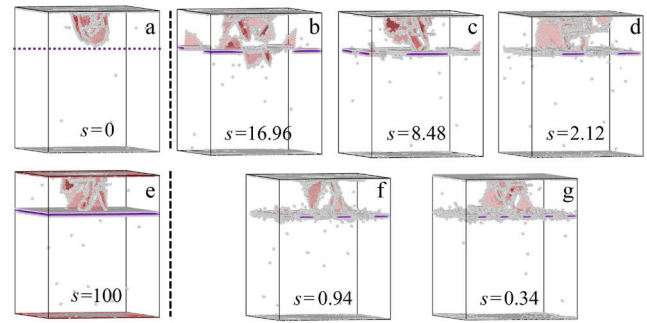

Fig.5 Microstructure evolution behavior of the initial dislocation nucleation beneath the indenter in Cu/graphene models with different graphene sizes: (a) s=0, (b) s=16.96, (c) s=8.48, (d) s=2.12, (e) s=100, (f) s=0.94, and (g) s=0.34
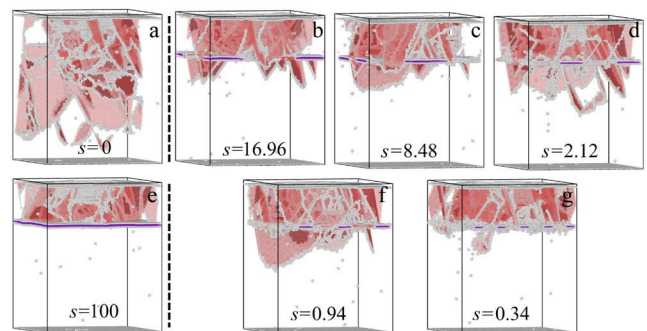

Fig.7 Microstructure evolution behavior at the indentation depth of 3.25 nm in Cu/graphene models with different graphene sizes: (a) s=0, (b) s=16.96, (c) s=8.48, (d) s=2.12, (e) s=100, (f) s=0.94, and (g) s=0.34
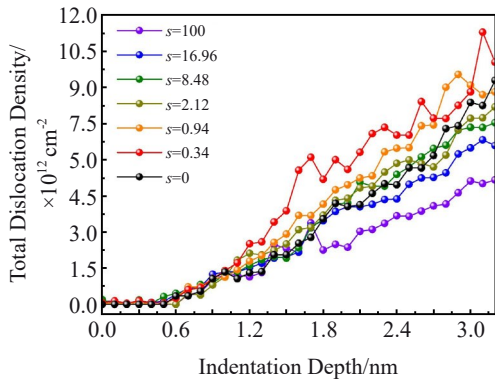
Fig.8 Total dislocation density versus indentation depth curves for different models

increasing trend of total dislocation density with decreasing graphene size *s*. According to the Taylor hardening equation[47], higher total dislocation density typically corresponds to higher strength (hardness). However, this relationship is not the case in above series of models. In the Cu/graphene model with a fully covered graphene interface, the total dislocation density is at the lowest level, and all dislocations are distributed above the graphene layer. Despite this, its hardness or average contact stress is higher than that of other models, indicating that the graphene layer effectively blocks dislocation motion. Although other Cu/graphene models exhibit higher total dislocation densities, their hardness/average contact stress is generally lower than that of the graphene fully covered model, suggesting that there must be some dislocation-induced weakening deformation behavior. Furthermore, the Cu/graphene model with *s*=8.48 exhibits the best mechanical properties, but its total dislocation density is at a moderate level and higher than that of the fully covered graphene interface model. Additionally, dislocations are observed both above and below the graphene sheets in model with *s*=8.48, indicating that the strengthening mechanisms in this model include not only the dislocation blocking effect of the graphene layer but also the additional strengthening effect from the extra dislocations.

Further observation and analysis of the microstructure during the indentation process reveal a significant number of immobile dislocations. Immobile dislocations typically contribute to material strengthening[48]. The variation in immobile dislocation density during the indentation process for different models is plotted in Fig. 9. Fig. 9a shows the variation of immobile dislocation density throughout the indentation process. The Cu/graphene composite with *s*=16.96 has the most immobile dislocations after the indentation is over, which is consistent with the observed significant immobile dislocations under the graphene sheet in Fig. 7, indicating that immobile dislocations play a prominent role in the deformation process. For model with *s*=8.48, the immobile dislocation content is at a moderate level, indicating that strengthening behavior due to immobile dislocations is involved. The Cu/graphene model with fully covered
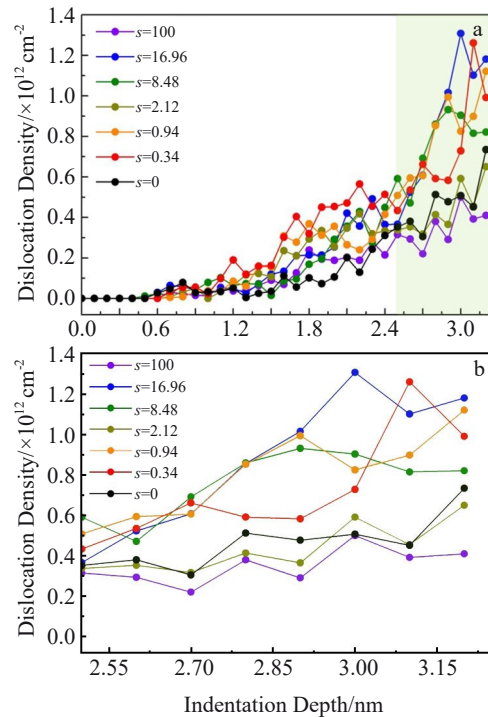

Fig.9 Changes of immobile dislocation density with indentation depth throughout the indentation process (a) and enlarged view of the shaded part in Fig.9a (b)

graphene interface has a minimal number of immobile dislocations, so the corresponding strengthening effect is also minimal. Additionally, in the two models with the graphene size less than *s*=8.48, i. e., *s*=0.94 and *s*=0.34, the immobile dislocation density increases sharply during the final indentation process, which is slightly lower than that of the model with *s*=16.96 but higher than that of the model with *s*=8.48. This indicates that immobile dislocation strengthening behavior is also involved in the final indentation process. Referring to Fig. 7, it is observed that almost no immobile dislocations are present below the graphene sheets, indicating that the immobile dislocations at this stage mainly result from the interaction of dislocations above the graphene sheets.

2.3 Effect of graphene sheet size on plastic deformation mechanisms of Cu/graphene composites

Detailed analysis of the plastic deformation behavior in different Cu/graphene models is conducted to elucidate the strengthening mechanisms of composites which are affected by the size of graphene sheet. The analysis is mainly considered from two aspects: (1) the impact of changes in graphene sheet size on its own deformation behavior and performance; (2) the impact of changes in graphene sheet size on the overall deformation behavior of the Cu/graphene composites. The possible strengthening mechanisms of the graphene layer in Cu/graphene models are analyzed[49–50], such as the hindrance/obstruction of dislocation motion and load-bearing effect, as well as second-phase strengthening mechanisms (dislocation bypassing or dislocation cutting mechanisms). Both types of strengthening mechanisms are

dependent on the size of the graphene sheet. For the former mechanism, larger graphene sheet results in better strengthening effects. For the latter mechanism, if it is related to dislocation bypassing mechanism, the strengthening effect increases with decreasing graphene sheet size/spacing[50]. However, if it is related to dislocation cutting mechanism, the strengthening effect decreases with decreasing graphene sheet size.

2.3.1   Deformation behavior in graphene layer

Wang's[27] calculations indicate that the size of graphene sheet affects the bending stiffness of the graphene plane, i.e., smaller sizes make the graphene layer more prone to bending or wrinkling. Fig. 10 shows the top and side views of the graphene sheet configurations at the maximum indentation depth for each model. The graphene atoms are colored according to their height along z-axis, with blue and red corresponding to the low and high positions, respectively. In the Cu/graphene composite with fully covered graphene interface (Fig. 10a), the graphene layer evolves into a somewhat undulating plane after interacting with dislocations. The red, green and blue regions indicate the high, intermediate and low areas of the graphene sheet, respectively. Detailed measurements of Fig. 10a show that the amplitude of the wrinkles in the transition regions between high and low locations of the graphene remains within the elastic deformation, without forming steps. The triangular green area in the graphene sheet corresponds to the trace lines left by dislocations sliding in the active slip systems in fcc crystal structure[48]. The color transitions to blue towards the center, indicating intense interaction with dislocations, resulting in large elastic deformation of the graphene, which implies that the graphene sheet consistently acts as a barrier to dislocation motion. When the graphene sizes are s=16.96 and s=8.48
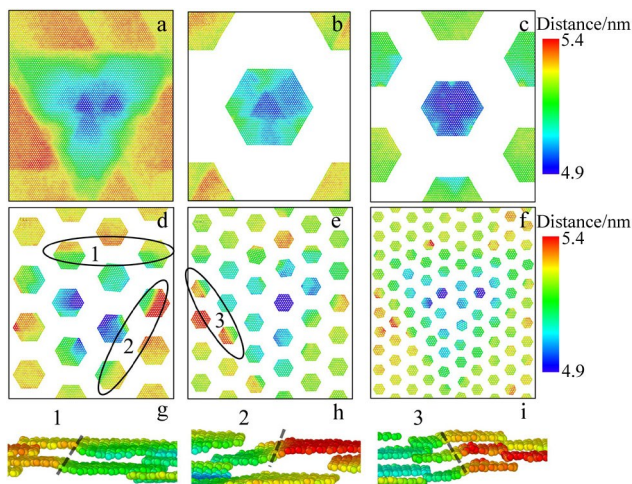
(Fig. 10b and 10c), the plane heights of the small graphene sheets are relatively uniform at the maximum indentation depth, without obvious high and low regions. As the graphene size decreases to s=2.12 and s=0.94 (Fig. 10d and 10e), some small graphene sheets form distinct high and low regions, marked by black ellipses (regions 1, 2 and 3). The side views of these regions are shown in Fig. 10g–10i, indicating severe deformation of the small graphene sheets. Measurements of their heights reveal step heights equivalent to the Burgers vector (indicated by the black dashed lines). These steps on the graphene sheets are likely due to the dislocation cutting strengthening mechanism, which aligns with the observation that smaller graphene sheets are more prone to out-of-plane wrinkling and bending. When the graphene size is reduced to s=0.34 (Fig. 10f), the plane heights of the small graphene sheets are relatively uniform. Observations of the micro-structure at this stage reveal that almost all the spacings between the graphene sheets in the model are occupied by stacking faults or dislocation networks, forming a morphology similar to that of fully covered graphene interface. Therefore, due to the coordinated deformation of the entire graphene layer, the unevenness or wrinkling of the individual small graphene sheet becomes less pronounced.

2.3.2   Deformation behavior in Cu/graphene composites

The impact of changes in graphene sheet size on the overall deformation behavior of the Cu/graphene composites is analyzed. Fig. 11 presents the deformation microstructures, in which typical deformation behavior is marked by ellipses. Dislocations, stacking faults and other defects appear at the maximum indentation depth for Cu/graphene composites with different graphene sheet sizes. These figures are colored by DXA, with purple lines representing stair-rod immobile dislocation and mesh structure representing the surface or Cu/graphene interface. The stacking fault (i. e., hcp structure atoms) is retained, while other atoms are removed, and exposure treatment is used for clearly observing the deformation behavior. Analysis reveals that all models involve the behavior of graphene load-bearing and dislocation blocking related interface strengthening.

Fig.11a shows the deformation behavior of the Cu/graphene

Fig.10 Top views of graphene sheet configuration in different Cu/graphene composites at maximum indentation depth: (a) s=100, (b) s=16.96, (c) s=8.48, (d) s=2.12, (e) s=0.94, and (f) s=0.34; enlarged side views of area 1 in Fig. 10d (g), area 2 in Fig.10d (h), and area 3 in Fig.10e (i)
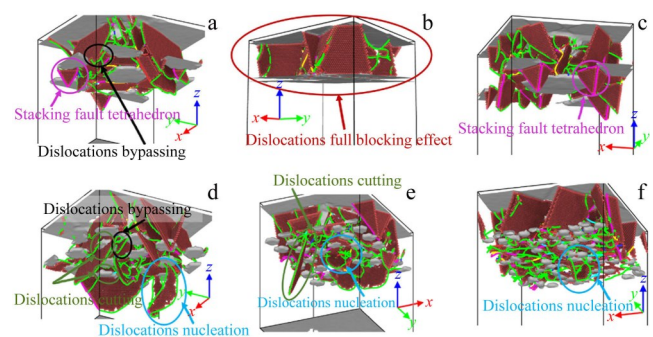

Fig.11 Deformation microstructures in different Cu/graphene models at the maximum indentation depth: (a) s=8.48, (b) s=100, (c) s=16.96, (d) s=2.12, (e) s=0.94, and (f) s=0.34

composite with s=8.48, where stacking fault tetrahedra formed by stair-rod immobile dislocations and dislocation bypassing behavior in the graphene sheet spacing are observed below the graphene sheets. In the Cu/graphene composite with fully covered graphene interface (Fig. 11b), it is evident that the graphene sheets completely block/pin dislocation motion, and dislocations are only present above the graphene sheet, which is consistent with the previously mentioned relatively low total dislocation density. In Cu/graphene composite with s= 16.96 (Fig. 11c), many stacking fault tetrahedra formed by stair-rod immobile dislocations are observed, corresponding to the highest immobile dislocation density mentioned earlier. When the graphene size is smaller than s=8.48, like in the model with s=2.12 (Fig.11d), several deformation behavior is observed, including dislocation bypassing the graphene sheets, dislocation nucleation under the graphene sheets and dislocation cutting through the graphene sheets. As the graphene sheet size further decreases, in the model with s= 0.94 (Fig.11e), the dislocation bypassing behavior between the graphene sheet spacing disappears, but the aforementioned dislocation nucleation under the graphene sheets and dislocation cutting through the graphene sheets are still observed. In the Cu/graphene model with s=0.34 (Fig.11f), the dislocation cutting through the graphene sheets further disappears, and thus only the dislocation nucleation and emission under the graphene sheets are observed. This is because the interface structure at this condition resembles the morphology of fully covered graphene interface, making it difficult for dislocations to emit beneath the indenter to slip through this interface. Many dislocations accumulate above the graphene sheets, leading to localized stress concentration at the interface. However, for model with s=0.34, the interface does not have the same high stress-bearing capacity as that of fully covered graphene interface, resulting in stress release through dislocation nucleation and emission under the graphene sheets. Therefore, the combined effect of these factors leads to a higher total dislocation density in model with s=0.34, consistent with the previously mentioned results in Fig. 9a, and the sharp increase in immobile dislocation density in the later stage of indentation may also result from the complex interactions between dislocations in the region above the graphene sheets.

2.3.3 Graphene size dependent strengthening mechanisms in Cu/graphene composites

The reasons for the transition of the plastic deformation mechanisms of the Cu/graphene composites due to changes in graphene sheet size are further analyzed. For the Cu/graphene composite with fully covered graphene interface, when dislocations emitted beneath the indenter interact with the graphene sheets, the high elastic modulus and intrinsic strength of graphene lead to complete blocking of dislocation motion. Dislocations continuously accumulate above the graphene sheet, forming pile-up groups and entanglements. This reduces the mean free path of dislocation motion and increases the resistance to dislocation movement, leading to

material strengthening. As the dislocations continue to increase, the number of dislocations above the graphene sheet approaches the storage capacity of dislocations. Consequently, the strengthening effect due to dislocation pile-up may be weakened compared to that at earlier stage, and stronger strengthening effect arises from the interactions between dislocations.

For Cu/graphene composites with varying graphene sheet sizes, several factors contribute to the overall deformation mechanisms. (1) Due to the non-periodic presence of graphene sheets within the model, the edges of the Cu/ graphene interface serve as preferred dislocation sources[51]. In the early stage of indentation, dislocations can nucleate and are emitted from these edges, releasing stress and causing some weakening. As indentation progresses, dislocation interactions become more intense, and the stress at the edge of the Cu/graphene interface is high, activating multiple slip systems. Then, the emitted partial dislocations are easy to interact to form immobile stacking fault tetrahedra, hindering dislocation motion and strengthening the material. In addition, the formation of stacking fault tetrahedra is affected by the spacing between graphene sheets, requiring sufficient space for partial dislocations to interact and to evolve. As the graphene sheet size decreases, corresponding to reduced graphene sheet spacing, the stacking fault tetrahedra below the graphene sheets gradually disappear. (2) The graphene sheets play a role in obstructing dislocation motion. In the early stage of indentation, the reduction in graphene sheet size weakens both the dislocation blocking and load-bearing effects, resulting in a weaker strengthening effect compared to fully covered model. In the later stage, as the dislocations above the graphene sheets accumulate to a high storage amount, the overall stress level increases. At this point, the weak regions between graphene sheet spacing act as a channel for dislocation slip. When s reduces from 8.48 to 0.94, the dislocation behavior transitions from dislocation bypassing to dislocation cutting through smaller graphene sheets, providing additional strengthening effects. Both dislocation bypassing and dislocation cutting mechanisms exist in the model with s=2.12, indicating that the critical size of the graphene sheets affecting the transition of the above deformation mechanisms is around this size. As the graphene sheet size decreases, the dislocation cutting strengthening mechanism weakens. (3) When the graphene size is reduced to s=0.34, the proportion of Cu/graphene interface edges becomes very large. During deformation, the spacing between graphene sheets is easily filled with stacking faults or dislocation networks emitted from the Cu/graphene interface edges, forming a morphology similar to that of fully covered graphene interface. Consequently, dislocation nucleation occurs at stress concentration regions below the graphene sheets. Therefore, changes in graphene sheet size lead to different dislocation behavior, resulting in varying strengthening behavior in terms of overall hardness and average contact stress of the Cu/graphene composites. The relationship between plastic deformation mechanisms and

hardness/average contact stress in the Cu/graphene models with different graphene sheet sizes is plotted in Fig.12, which illustrates the deformation mechanisms in these models.

In summary, for the Cu/graphene composite with fully covered graphene interface, the graphene dislocation blocking and load-bearing effects are the dominant strengthening mechanisms. However, the limited mean free path of dislocation motion restricts the full exertion of the dislocation blocking effect, resulting in less comprehensive strengthening effect compared to the model with s=8.48. When the graphene size reduces to s=16.96, the graphene load-bearing and dislocation blocking related interface strengthening effects become weaker than those in the fully covered model but still play the main strengthening roles. Moreover, stacking fault tetrahedra also contribute to the enhancement in hardness. When the graphene size further reduces to s=8.48, despite of graphene load-bearing and dislocation blocking related interface strengthening mechanisms, stacking fault tetrahedra still exert strengthening effect, the dominant strengthening behavior changes to the dislocation bypassing mechanism due to smaller distributed graphene size and smaller graphene sheet spacing, and thus the hardness/average contact stress of the model is the highest. With decreasing the graphene sheet size, the deformation mechanisms transition from stacking fault tetrahedra, dislocation bypassing and dislocation cutting to dislocation nucleation in turn. For other models with different graphene sheet sizes, both strengthening and weakening mechanisms are involved, including the size-dependent dislocation blocking and load-bearing strength-ening effect of the graphene sheets. Specifically, the models with s=2.12 and s=0.94 exhibit a combination of dislocation cutting strengthening mechanism and dislocation interface nucleation softening mechanism, and the former has an additional dislocation bypassing mechanism. The model with s=0.34 shows significant dislocation interface nucleation softening mechanism, resulting in less effective strengthening compared with fully covered model. Overall, this study indicates that there is an optimal graphene sheet size that
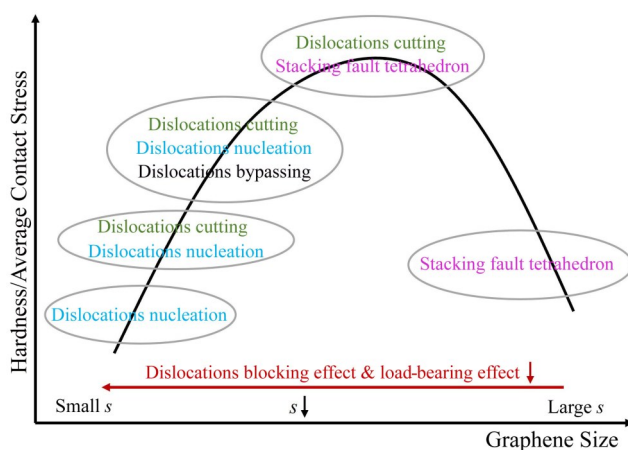
maximizes the overall hardness of the Cu/graphene composites.

3 Conclusions

1) Changes in the size of the graphene sheet can significantly affect the hardness of Cu/graphene composites. When the size of the sheet layer is s=8.48, the Cu/graphene composite exhibits the highest hardness, indicating that the Cu/graphene composite with partial coverage can achieve higher hardness than the model with full graphene coverage.

2) In addition to the obstruction of dislocations by the graphene sheet and the graphene load-bearing effect, the dislocation bypassing and stacking fault tetrahedra pinning dislocation mechanism provide extra strengthening effects.

3) Graphene sheet size plays a critical role in determining the hardness and deformation behavior of the Cu/graphene composites.

References

1 Papageorgiou D G, Kinloch I A, Young R J. *Progress in Materials Science*[J], 2017, 90: 75

2 Yang M, Liu Y, Fan T *et al. Progress in Materials Science*[J], 2020, 110: 100652

3 Wang Q J, Fan R X, Liu Dan *et al. Rare Metal Materials and Engineering*[J], 2022, 51(2): 414

4 Wang X D, Zhou H, Sun P *et al. Rare Metal Materials and Engineering*[J], 2023, 52(1): 81

5 Liu J, Ding R, Cao J *et al. Carbon*[J], 2024, 228: 119382

6 Zhang X, Zhao N, He C. *Progress in Materials Science*[J], 2020, 113: 100672

7 Yang Z, Wang D, Lu Z *et al. Applied Physics Letters*[J], 2016, 109(19): 191909

8 Zhao L, Guo Q, Li Z *et al. International Journal of Plasticity*[J], 2019, 116: 265

9 Huang J, Li M, Chen J *et al. Materials*[J], 2023, 16(7): 2722

10 Vardanyan V H, Urbassek H M. *Carbon*[J], 2021, 185: 660

11 Chen X, Zhao D, Rong X *et al. Carbon*[J], 2024, 228: 119419

12 Shuang F, Dai Z, Aifantis K E. *ACS Applied Materials & Interfaces*[J], 2021, 13(22): 26610

13 Jiang Yuqian, Zhang Xiang, Zhao Naiqin *et al. Materials China*[J], 2023, 42(12): 959 (in Chinese)

14 Yang Changyi, Wu Shufan, Xiao Wenlong *et al. Materials China*[J], 2024, 43(3): 195 (in Chinese)

15 Li J, Zhang X, Qian M *et al. Composites Part A: Applied Science and Manufacturing*[J], 2023, 166: 107410

16 Zhao M, Xiong D B, Tan Z *et al. Scripta Materialia*[J], 2017, 139: 44

17 Yang X, Yang L, Zhu D *et al. Journal of Materials Research and Technology*[J], 2024, 28: 3286

18 Chen X, Rong X, Zhao D *et al. Scripta Materialia*[J], 2023, 222: 115037

19 Chen B, Shen J, Ye X *et al. Acta Materialia*[J], 2017, 140: 317

Fig.12 Plastic deformation mechanisms in models with different graphene sheet sizes

20 Chen X, Tao J, Liu Y *et al. Carbon*[J], 2019, 146: 736

21 Shuang F, Aifantis K E. *Carbon*[J], 2021, 172: 50

22 Huang Y, Yang Z, Lu Z. *Computational Materials Science*[J], 2021, 186: 109969

23 Qiu Z, Zhang Z, Xiong Y *et al. Applied Surface Science*[J], 2022, 596: 153546

24 Cao H Y, Guo Z X, Xiang H *et al. Physics Letters A*[J], 2012, 376(4): 525

25 Chu Y, Ragab T, Basaran C. *Computational Materials Science*[J], 2014, 81: 269

26 Georgantzinos S K, Giannopoulos G I, Katsareas D E *et al. Computational Materials Science*[J], 2011, 50(7): 2057

27 Wang Q. *Physics Letters A*[J], 2010, 374(9): 1180

28 Dong J, Geng D, Liu F *et al. Angew Chem Int Ed Engl*[J], 2019, 58(23): 7723

29 Zeng M, Wang L, Liu J *et al. Journal of the American Chemical Society*[J], 2016, 138(25): 7812

30 Wang L, Yang Z, Cui Y *et al. Scientific Reports*[J], 2017, 7: 41896

31 Foiles S M, Baskes M I, Daw M S. *Physical Review B*[J], 1986, 33(12): 7983

32 Zhang S, Wang F, Huang P. *Journal of Materials Science & Technology*[J], 2021, 87: 176

33 Zhang S, Huang P, Wang F. *Materials & Design*[J], 2020, 190: 108555

34 Stuart S J, Tutein A B, Harrison J A. *The Journal of Chemical Physics*[J], 2000, 112(14): 6472

35 Guo S J, Yang Q S, He X Q *et al. Compos Part B Eng*[J], 2014, 58: 586

36 Stukowski A. *Modelling and Simulation in Materials Science and Engineering*[J], 2010, 18(1): 015012

37 Faken D, Jónsson H. *Computational Materials Science*[J], 1994, 2(2): 279

38 Falk M L, Langer J S. *Physical Review E*[J], 1998, 57: 7192

39 Shimizu F, Ogata S, Li J. *Materials Transactions*[J], 2007, 48(11): 2923

40 Stukowski A, Bulatov V V, Arsenlis A. *Modelling and Simulation in Materials Science and Engineering*[J], 2012, 20(8): 085007

41 Plimpton S. *Journal of Computational Physics*[J], 1995, 117: 1

42 Vardanyan V H, Urbassek H M. *Proceedings of the 3rd Conference on Physical Modeling for Virtual Manufacturing Systems and Processes*[C]. Amsterdam: Springer, 2023: 51

43 Fu T, Peng X, Chen X *et al. Scientific Reports*[J], 2016, 6(1): 35665

44 Nair A K, Parker E, Gaudreau P *et al. International Journal of Plasticity*[J], 2008, 24(11): 2016

45 Zhang Y, An Q, Li J *et al. J Mol Model*[J], 2020, 26(12): 335

46 Zhu P Z, Fang F Z. *Applied Physics A*[J], 2012, 108(2): 415

47 Sanaty-Zadeh A. *Materials Science and Engineering A*[J], 2012, 531: 112

48 Hirth J P, Lothe J. *Theory of Dislocations (2nd Ed)* [M]. New York: John Wiley & Sons Inc, 1982: 757

49 Zhao C, Zhou J, Zhong K *et al. Computational Materials Science*[J], 2024, 239: 112993

50 Sheinerman A G. *Critical Reviews in Solid State and Materials Sciences*[J], 2021, 47(5): 708

51 Yazdandoost F, Yari Boroujeni A, Mirzaeifar R. *Physical Review Materials*[J], 2017, 1(7): 076001

铜/石墨烯复合材料中石墨烯尺寸依赖的硬度及强化机制：分子动力学研究

张　霜[1]，常　国[1]，李　亮[1]，李　响[1]，彭浩然[1]，陈凯运[1]，杨　楠[2]，霍望图[1]

(1. 西北有色金属研究院 先进材料研究所，陕西 西安 710016)

(2. 西部金属材料股份有限公司 联合技术中心，陕西 西安 710201)

摘　要：金属/石墨烯复合材料的卓越强度在很大程度上取决于石墨烯的特征尺寸、分布和形态。然而，石墨烯尺寸/分布对力学性能及相关强化机制的影响尚未完全阐明。在相同的石墨烯体积分数和分布条件下，通过分子动力学模拟研究了石墨烯片尺寸对复杂应力场下铜/石墨烯复合材料硬度和变形行为的影响，并建立单晶铜和石墨烯完全覆盖的铜基复合材料的2种模型作为对照。结果表明，强化效果随着石墨烯片尺寸的变化而变化。除了石墨烯位错阻挡效应和承载效应外，随着石墨烯片尺寸减小，变形机制依次从层错四面体、位错绕过、位错切过向位错形核变形机制转变。石墨烯片未完全覆盖铜基体的铜/石墨烯复合材料的硬度甚至高于完全覆盖的复合材料。经分析，位错挤出机制和汤普森四面体钉扎位错机制提供了额外的强化效应。

关键词：铜/石墨烯复合材料；石墨烯尺寸；硬度；强化机制；分子动力学